A sensitivity equation method for fast evaluation of nearby flows and uncertainty analysis for shape parameters

Régis Duvigneau, Dominique Pelletier

A sensitivity equation method for fast evaluation of nearby flows and uncertainty analysis for shape parameters

R. DUVIGNEAU * & D. PELLETIER †

* INRIA Opale Project-Team

2004 route des lucioles, 06902 Sophia-Antipolis, FRANCE

† Département de Génie Mécanique, Ecole Polytechnique de Montréal

Montréal (Québec), CANADA, H3C 3A7

A paper submitted to the International Journal for Computational Fluid Dynamics

Corresponding author:

Régis Duvigneau

INRIA Sophia-Antipolis

Projet OPALE

2004 route des lucioles, BP 93, 06902 Sophia-Antipolis

FRANCE

Regis.Duvigneau@sophia.inria.fr

Tel: +33 4 92 38 71 77

Fax: +33 4 92 38 79 80

Abstract

This paper presents the application of the Continuous Sensitivity Equation Method (CSEM) to fast evaluation of nearby flows and to uncertainty analysis for shape parameters. The flow and sensitivity fields are solved using an adaptive finite-element method. A new approach is presented to extract accurate flow derivatives at the boundary, which are needed in the shape sensitivity boundary conditions. Boundary derivatives are evaluated via high order Taylor series expansions used in a constrained least-squares procedure. The proposed method is first applied to fast evaluation of nearby flows: the baseline flow and sensitivity fields around a NACA 0012 airfoil are used to predict the flow around airfoils with nearby shapes obtained by modifications of the thickness (NACA 0015), the angle of attack and the camber (NACA 4512). The method is then applied to evaluate the influence of geometrical uncertainties on the flow around a NACA 0012 airfoil.

keywords : Continuous Sensitivity Equation Method, fast evaluations of nearby flows, uncertainty analysis, sensitivity analysis

1 Introduction

Sensitivity analysis is used for a wide range of engineering problems, including characterization of complex flows, fast evaluation of nearby flows[1], optimal design[2], uncertainty analysis[3], etc... Indeed, availability of methods for fast evaluation of nearby flows provides a rigorous framework to answer some difficult questions. For instance: what is the effect on the flow of changing the angle of attack, the thickness or the camber of an airfoil ? First order Taylor series in parameter space yield quick and inexpensive estimates of the flow over the whole domain for nearby values of the shape parameter. Taylor series are very cost effective because the sensitivities can be solved for a fraction of the cost of the flow computation.

Sensitivity analysis is also a scientifically rigorous tool for assessing the effects of input data uncertainty such as manufacturing tolerances on the performance of an airfoil. In essence, sensitivity information allow us to cascade input data uncertainty through the CFD code to obtain uncertainty estimates of

the flow response. Here, uncertainty analysis will be performed using first order sensitivity information combined to first order statistics[4].

Functional sensitivity analysis in aerodynamics has been an active research topic for the last years. It has been intensively studied using ajoint methods for design optimization purpose (see for instance the works of Jameson *et al.* [5], Anderson and Venkatakrishnan [6], Elliott and Peraire [7], Giles *et al.* [8], Martins *et al.* [9], Mohammadi and Pironneau [10], Beux and Dervieux [11]). However, the computation of flow sensitivities using direct approaches, for fast evaluation of nearby flows or uncertainty analysis purpose, has been less reported in the literature. The present study is focused on this methodology.

Sensitivity information can be obtained in either of two ways. In the *approximate-then-differentiate* approach (often called Discrete Sensitivity Equation Method), the discrete form of the flow equations is differentiated and the total derivative of the flow discretization with respect to the design parameters is calculated. In the *differentiate-then-approximate* approach (known as the Continuous Sensitivity Equation Method CSEM), partial differential equations for the flow sensitivities are obtained by implicit differentiation of the equations governing the flow. They are then approximated numerically.

The CSEM is preferred for the present study, because it offers several advantages over the discrete sensitivity approach. In particular, since differentiation occurs before any discretization, the delicate computation of mesh sensitivities and all of the overhead associated with them is avoided. Consequently, the CSEM requires less memory and is computationaly less expensive than automatic differentiation, as shown by Borggaard and Verma[12]. Moreover, the CSEM is a natural approach when using adaptive methods: since the topology of the mesh changes with adaptation, mesh derivatives do not always exist, making the discrete sensitivity method ill-suited. Another advantage is that there is no requirement to use the same algorithm to approximate the CSE and the original PDE model. Thus, special algorithms may be constructed to take advantage of the linear structure of the CSE.

However, the main difficulty with the CSEM arises when one deals with shape parameters. In this particular case, flow gradients are required as source terms in the CSE and as coefficients in the boundary conditions for the CSE. Flow gradients in the interior of the computational domain can be computed

relatively easily and accurately by a local projection technique[13] (which is already used for error estimation). However, on general unstructured meshes, the accuracy of derivatives reconstructed in this way degrades significantly near the boundary[14]. This induces errors in the boundary conditions that result in poor solutions for the sensitivity fields[14] (the numerical solution often appears shifted from the exact solution by some fixed amount that varies from one problem to the next).

The current study presents a new approach to extract accurate boundary conditions of the CSE for shape parameters. It uses high order Taylor series expansions in conjunction with a constrained least-squares procedure. The proposed method is described in the first sections of the paper. Two applications are then presented. First, the CSEM is applied to fast evaluation of nearby flows via linear Taylor series in parameter space. The baseline flow and sensitivity fields around a NACA 0012 airfoil are used to evaluate the flow around an airfoil of nearby shape, by modifying in turn the airfoil thickness, the angle of attack and the camber. To validate the approach, the extrapolated flow is compared to a reanalysis of the flow around the airfoil of modified shape . In the second application, sensitivity fields are used to evaluate uncertainties of the flow fields due to geometrical uncertainties of the airfoil. Uncertainties on the thickness, angle of attack and camber cascade through the CFD code to obtain quantified uncertainty estimates of the flow response.

2 Flow equations

The flows of interest are described by the laminar steady Navier-Stokes equations. The momentum and mass conservation laws are written as:

$$\rho \mathbf{u} \cdot \nabla \mathbf{u} = -\nabla p + \nabla \cdot \tau(\mathbf{u}) + \mathbf{f}, \tag{1}$$

$$\nabla \cdot \mathbf{u} = 0, \tag{2}$$

where ρ is the density, $\mathbf{u}$ the velocity and p the pressure. Finally, $\mathbf{f}$ is a volumetric force. The viscous fluid stress is given by:

$$\tau(\mathbf{u}) = \mu \left\{ \nabla \mathbf{u} + (\nabla \mathbf{u})^T \right\}.$$

where μ is the viscosity of the fluid.

Dirichlet and Neumann boundary conditions are imposed on boundaries Γ_D and Γ_N respectively:

$$\mathbf{u} = \overline{\mathbf{u}} \quad (\Gamma_D), \tag{3}$$

$$\left[-p\mathbf{I} + \mu\left(\nabla\mathbf{u} + (\nabla\mathbf{u})^T\right)\right] \cdot \hat{\mathbf{n}} = \overline{\mathbf{t}} \quad (\Gamma_N), \tag{4}$$

where $\hat{\mathbf{n}}$ is an outward unit vector normal to the boundary and $\mathbf{I}$ the second order identity tensor.

3 Continuous sensitivity equations

The continuous sensitivity equations (CSE) are derived formally by implicit differentiation of the flow equations (1)-(2) with respect to an arbitrary parameter a. Thus, we treat the variable $\mathbf{u}$ as a function of both space and parameter a. This dependence is denoted $\mathbf{u} = \mathbf{u}(\mathbf{x}; a)$. The flow sensitivities are defined as the following partial derivatives:

$$\mathbf{s_u} = \frac{\partial \mathbf{u}}{\partial a} \quad s_p = \frac{\partial p}{\partial a}. \tag{5}$$

Then, with no particular assumption on the nature of the parameter a, the general and generic form of the CSE governing the sensitivity fields are written as:

$$\rho'\mathbf{u}\cdot\nabla\mathbf{u} + \rho\left(\mathbf{s_u}\cdot\nabla\mathbf{u} + \mathbf{u}\cdot\nabla\mathbf{s_u}\right) = -\nabla s_p + \nabla\cdot\tau(\mathbf{s_u}) + \nabla\cdot S_\tau(\mathbf{u}) + \mathbf{f}', \tag{6}$$

$$\nabla\cdot\mathbf{s_u} = 0, \tag{7}$$

with:

$$S_\tau(\mathbf{u}) = \mu'\left\{\nabla\mathbf{u} + (\nabla\mathbf{u})^T\right\}.$$

$\mathbf{f}'$ is the sensitivity of $\mathbf{f}$ in equation (1) (i.e. the total derivative $\frac{D\mathbf{f}}{Da}$). The total derivatives of the fluid properties with respect to the parameter a are denoted using a ($'$). For instance:

$$\mu' = \frac{D\mu}{Da} = \frac{\partial\mu}{\partial a} + \frac{\partial\mu}{\partial\mathbf{u}}\cdot\mathbf{s_u} \tag{8}$$

To complete the description of the problem, the boundary conditions (3)-(4) are differentiated in the same manner. However, if a is a shape parameter, the position of boundary points is parameter dependent.

Then, the differentiation must account for the fact that both the boundary location and the value of the boundary condition depend on a. The differentiation of the Dirichlet boundary condition $\mathbf{u} = \overline{\mathbf{u}}$ on (Γ_D) leads to:

$$\begin{aligned} \frac{D\mathbf{u}}{Da} &= \frac{D\overline{\mathbf{u}}}{Da} \\ \frac{\partial \mathbf{u}}{\partial a} + \nabla \mathbf{u} \cdot \frac{\partial \mathbf{x}}{\partial a} &= \frac{D\overline{\mathbf{u}}}{Da} \end{aligned}$$

where D/Da denotes the total derivative with respect to a. The boundary condition for the sensitivity of $\mathbf{u}$ is finally:

$$\mathbf{s_u} = \frac{D\overline{\mathbf{u}}}{Da} - \nabla \mathbf{u} \cdot \frac{\partial \mathbf{x}}{\partial a} \quad (\Gamma_D^T) \tag{9}$$

Similar manipulations on Neumann boundary condition (4) yield:

$$\begin{aligned} &\left[-s_p \mathbf{I} + \mu \left(\nabla \mathbf{s_u} + (\nabla \mathbf{s_u})^T\right)\right] \cdot \hat{\mathbf{n}} \\ &\quad + \left[\mu' \left(\nabla \mathbf{u} + (\nabla \mathbf{u})^T\right)\right] \cdot \hat{\mathbf{n}} = \frac{D\overline{\mathbf{t}}}{Da} - \left\{\nabla \left[-p\mathbf{I} + \mu \left(\nabla \mathbf{u} + (\nabla \mathbf{u})^T\right)\right] \cdot \frac{\partial \mathbf{x}}{\partial a}\right\} \cdot \hat{\mathbf{n}} \\ &\qquad - \left[-p\mathbf{I} + \mu \left(\nabla \mathbf{u} + (\nabla \mathbf{u})^T\right)\right] \cdot \frac{\partial \hat{\mathbf{n}}}{\partial a} \quad (\Gamma_N^u), \end{aligned} \tag{10}$$

When shape parameters are considered, the first derivatives of the flow variables at the boundary are needed to evaluate Dirichlet boundary conditions for sensitivities (equation 9). First and second derivatives are required for Neumann boundary conditions for sensitivities (equation 10). This introduces significant numerical challenges and difficulties when solving the CSE. Since approximate boundary conditions are constructed from the finite-element solution for the flow field, inaccuracies in the boundary conditions will result in poor solutions for the sensitivity fields[14].

4 Numerical framework

4.1 Solver

The flow equations and the CSE are solved using an adaptive finite-element method [15, 16]. We discuss the salient features here for completeness and to set up the approximation of the above described CSE.

The weak form of the continuity, momentum and energy equations are formed, and a discretization based on the 7-noded Crouzeix-Raviart element leads to a system of nonlinear algebraic equations which are then solved using Newton's method.

The accuracy of any finite-element approximation is directly related to the element mesh size used in the computation. An adaptive remeshing procedure is employed to improve this approximation by refining the mesh in regions of rapid variations of the flow variables and coarsening it where the flow fields are smooth. The regions targeted for refinement are identified by using an error estimator based on local projections of discontinuous quantities onto a local continuous polynomial basis[13, 17]. For example, since the Crouzeix-Raviart element uses enriched quadratic bases for velocity, the stress tensor τ is discontinuous and piecewise linear for this approximation. We can define an error estimate by projecting these derivatives onto a continuous quadratic polynomial basis and by evaluating the norm of the difference between the reconstructed and finite-element derivatives.

Once error estimates are obtained for all dependent variables and their sensitivities, an optimal mesh is designed using the asymptotic rate of convergence of the finite-element method. An optimal mesh is generated which redistributes the mesh size so that each element bears the same contribution to the total error (i.e. equidistribution of the error norm). This process is repeated, beginning with a coarse mesh to produce progressively finer meshes, such that the error is reduced by a constant factor from one mesh to the next. Details of this adaptive remeshing procedure may be found in the literature[18].

4.2 Boundary conditions for CSE

As explained above, flow derivatives at the boundary are required to evaluate the CSE boundary conditions for shape parameters. The local projection of flow derivatives, used for errors estimation[13, 17], may be employed to provide the boundary derivatives. However, this approach yields poor results since projected derivatives usually exhibit low accuracy at the boundary[14]. To improve the evaluation of the flow derivatives at the boundary, we propose to use a least squares technique combined with high order Taylor series expansions around each boundary vertex. The method to extract flow derivatives using

a least-squares method was demonstrated by Fortin *et al.*[19]. We innovate by enforcing constraints on the least-squares method to ensure that the Taylor series are consistent with the imposed boundary conditions.

For the sake of simplicity, the proposed method is presented for a generic flow variable ϕ. The truncated Taylor series expansion of order k for ϕ around a boundary node $P(x_P, y_P)$ reads:

$$\begin{aligned}\phi(x,y) &= \phi(x_P,y_P) + (x-x_P)\phi_x + (y-y_P)\phi_y \\ &\quad + \frac{1}{2}(x-x_P)^2\phi_{xx} + (x-x_P)(y-y_P)\phi_{xy} + \frac{1}{2}(y-y_P)^2\phi_{yy} + \ldots \end{aligned} \tag{11}$$

in which ϕ and its derivatives are the unknowns. Their values are determined by matching, in a least-squares sense, the value of the Taylor series to that of the flow variable at a set of points $N(x_N, y_N)$ within a patch $\mathcal{P}$ surrounding the node P. This corresponds to solving the following overdetermined rectangular system of equations:

$$\phi_N = \mathbf{B}^T \mathbf{y}_\phi \quad \forall N \in \mathcal{P} \tag{12}$$

where:

$$\phi_N = \phi(x_N, y_N) \tag{13}$$

$$\mathbf{B}^T = \{1 \quad x_N - x_P \quad y_N - y_P \quad \frac{1}{2}(x_N - x_P)^2 \quad (x_N - x_P)(y_N - y_P) \quad \frac{1}{2}(y_N - y_P)^2 \ \ldots\} \tag{14}$$

$$\mathbf{y}_\phi^T = \{\phi \quad \phi_x \quad \phi_y \quad \phi_{xx} \quad \phi_{xy} \quad \phi_{yy} \ \ldots\}_P \tag{15}$$

To determine $\mathbf{y}_\phi$, a discrete least-squares problem is solved by minimizing the square of the distance between the Taylor series and the value of the variable at the N mesh nodes in the patch $\mathcal{P}$. That is we minimize the quadratic form $\mathcal{J}(\mathbf{y}_\phi)$:

$$\text{Min } \mathcal{J}(\mathbf{y}_\phi) = \frac{1}{2} \sum_{N \in \mathcal{P}} (\mathbf{B}^T \mathbf{y}_\phi - \phi_N)^2 \tag{16}$$

The boundary condition for ϕ at node P is either a Dirichlet condition $\phi = \overline{\phi_P}$ or a Neumann condition $\nabla\phi \cdot \hat{n} = \overline{q}_P$. However, there is no guarantee that the Taylor series (11) evaluated at the boundary node P will match the boundary condition. Further accuracy improvements are achieved if the least-squares

solution $\mathbf{y}_\phi$ is constrained to match the value of the boundary condition at node P. This is done by considering the boundary condition as a constraint on the least-squares problem.

In the case of a Dirichlet boundary condition $\phi = \overline{\phi}_P$, we now minimize $\mathcal{J}(\mathbf{y}_\phi)$ subject to $\mathbf{y}_\phi(1) = \overline{\phi}_P$. The constraint is enforced by introducing a Lagrange multiplier l_ϕ and the Lagrangian functional:

$$\mathcal{L}_D(\mathbf{y}_\phi, l_\phi) = \frac{1}{2} \sum_{N \in \mathcal{P}} (\mathbf{B}^T \mathbf{y}_\phi - \phi_N)^2 + l_\phi (\mathbf{D}_\phi^T \mathbf{y}_\phi - \overline{\phi}_P), \tag{17}$$

where $\mathbf{D}_\phi^T = \{1\,0\,0\,\ldots\,0\}$. The solution of this contrained problem is characterized by stationnary conditions for the Lagrangian with respect to the unknown $\mathbf{y}_\phi$ and the Lagrange multiplier l_ϕ. The derivatives of the functional can be expressed as:

$$\begin{aligned} \frac{\partial}{\partial \mathbf{y}_\phi} \mathcal{L}_D &= \sum_{N \in \mathcal{P}} \mathbf{B}(\mathbf{B}^T \mathbf{y}_\phi - \phi_N) + l_\phi \mathbf{D}_\phi, \\ \frac{\partial}{\partial l_\phi} \mathcal{L}_D &= \mathbf{D}_\phi^T \mathbf{y}_\phi - \overline{\phi}_P. \end{aligned} \tag{18}$$

Then, by setting the derivatives (18) to zero, we obtain the following linear system for $\mathbf{y}_\phi$:

$$\begin{bmatrix} \sum_{N \in \mathcal{P}} \mathbf{B}\mathbf{B}^T & \mathbf{D}_\phi \\ \mathbf{D}_\phi^T & 0 \end{bmatrix} \begin{Bmatrix} \mathbf{y}_\phi \\ l_\phi \end{Bmatrix} = \begin{Bmatrix} \sum_{N \in \mathcal{P}} \mathbf{B}\phi_N \\ \overline{\phi}_P \end{Bmatrix}, \tag{19}$$

whose solution is obtained by LU factorization. In the case of a Neumann boundary condition $\nabla\phi \cdot \hat{n} = \overline{q}_P$, we now minimize the quadratic form $\mathcal{J}(\mathbf{y}_\phi)$ subject to $\mathbf{y}_\phi(2)\hat{n}_x + \mathbf{y}_\phi(3)\hat{n}_y = \overline{q}_P$. The Lagrangian functional is:

$$\mathcal{L}_N(\mathbf{y}_\phi, l_\phi) = \frac{1}{2} \sum_{N \in \mathcal{P}} (\mathbf{B}^T \mathbf{y}_\phi - \phi_N)^2 + l_\phi (\mathbf{N}_\phi^T \mathbf{y}_\phi - \overline{q}_P). \tag{20}$$

with $\mathbf{N}_\phi^T = \{0,\ \hat{n}_x\,\hat{n}_y,\ 0,\ \ldots\,0\}$. As above, the solution of the contrained problem is characterized by stationnary conditions for the Lagrangian. The derivatives read:

$$\begin{aligned} \frac{\partial}{\partial \mathbf{y}_\phi} \mathcal{L}_N &= \sum_{N \in \mathcal{P}} \mathbf{B}(\mathbf{B}^T \mathbf{y}_\phi - \phi_N) + l_\phi \mathbf{N}_\phi, \\ \frac{\partial}{\partial l_\phi} \mathcal{L}_N &= \mathbf{N}_\phi^T \mathbf{y}_\phi - \overline{q}_P. \end{aligned} \tag{21}$$

Then, the extremum corresponds to the solution of the following linear system:

$$\begin{bmatrix} \sum_{N \in \mathcal{P}} \mathbf{B}\mathbf{B}^T & \mathbf{N}_\phi \\ \mathbf{N}_\phi^T & 0 \end{bmatrix} \begin{Bmatrix} \mathbf{y}_\phi \\ l_\phi \end{Bmatrix} = \begin{Bmatrix} \sum_{N \in \mathcal{P}} \mathbf{B}\phi_N \\ \overline{q}_P \end{Bmatrix}, \tag{22}$$

The vector $\hat{\mathbf{n}}$ at each vertex node is defined using the weighted mean of the neighboring vectors at mid-side node (figure 1).

When the variable ϕ considered is a velocity component, the Neumann boundary condition involves the pressure and the first derivatives of the two velocity components. Therefore, the three least-squares problems for u, v and p must be solved in a coupled manner for the two velocity components and the pressure to ensure that Taylor series for u, v, and p are consistent with the Neumann boundary conditions imposed on the flow.

Once problems (19) and (22) are solved, first and second boundary derivatives are extracted from vector $\mathbf{y}_\phi$: $\mathbf{y}_\phi(2) = \phi_x$, $\mathbf{y}_\phi(3) = \phi_y$, $\mathbf{y}_\phi(4) = \phi_{xx}$ etc ... and used to evaluate the boundary conditions for the CSE, described by equations (9) and (10).

There remain two issues to discuss: choosing the order of the Taylor series expansions and selecting the extent of the patch on which the least-squares problem is solved. To describe the patch, we introduce the concept of an l-layer patch. A 1-layer patch includes all elements that are connected to a given node P, a 2-layer patch includes elements which are connected to elements of the 1-layer patch of node P, etc. Figure 2 provides two examples of 2-layer patches, one for a vertex node and another for a mid-side node. Numerical experiments performed for simple flow solutions, generated by the Method of Manufactured Solutions[20] (MMS), show that 5th order Taylor series expansions (or higher) and 6-layer patches (or bigger) are required to extract boundary derivatives ensuring accurate boundary conditions for the CSE[1]. Particularly, it is shown that the boundary flow gradients obtained using this least-squares approach are far more accurate than those obtained by local projection[1]. Under these conditions, the error estimator for the sensitivity fields converges towards the true error as the mesh is refined and the asymptotic exactness of the sensitivity fields is established. This implies that the accuracy and reliability of both the solution and its error estimates improve as the mesh is refined.

5 Application to evaluation of nearby flow solutions

5.1 Problem description

We apply the method to airfoils at low Reynolds numbers. We use sensitivity information to estimate solutions for airfoils of nearby shape. The flow around a NACA 0012 airfoil at a Reynolds number $Re = 2000$ and an angle of attack of $\alpha = 5^\circ$ is used as a baseline. The configuration of the problem is described on figure 3. Dirichlet boundary conditions are imposed at the inflow and on the airfoil surface, and homogeneous Neumann boundary conditions are prescribed as far field conditions. The distance between the trailing edge and the outlet boundary is large enough (about 10 chords) to ensure that homogeneous Neumann boundary conditions are a good approximation and that its location does not affect the results. All the results provided below are expressed in terms of non-dimensional values.

The airfoil thickness, the angle of attack and the camber are considered in turn as shape parameters. The boundary conditions for the CSE specific to t, α and γ are detailed in appendix. For a given parameter a, solutions at nearby values of the parameter are obtained by evaluating a linear Taylor series in a-space, using the flow and sensitivity data from the baseline solution. The following expressions are used for fast and inexpensive evaluation of flows around an airfoil of modified shape:

$$\begin{aligned} u_{\text{extr}} &\approx u_{\text{NACA 0012}} + \left(\frac{\partial u}{\partial a}\right) \times \Delta a \\ v_{\text{extr}} &\approx v_{\text{NACA 0012}} + \left(\frac{\partial v}{\partial a}\right) \times \Delta a \\ p_{\text{extr}} &\approx p_{\text{NACA 0012}} + \left(\frac{\partial v}{\partial a}\right) \times \Delta a \end{aligned} \tag{23}$$

To illustrate the capability of the proposed method to evaluate accurate sensitivity fields, the extrapolated flow fields are compared to a reanalysis of the flow around the airfoil of modified shape. Notice that the extrapolated flow fields are computed and plotted on the baseline geometry, not on the modified airfoil. In the following sections we present results for sensitivity analysis with respect to the thickness, the angle of attack and the camber parameters.

5.2 Thickness

Points on the surface of a NACA 0012 airfoil verify the following equation:

$$y = \pm 5t(0.2969\sqrt{x} - 0.1260x - 0.3537x^2 + 0.2843x^3 - 0.1015x^4) \quad x \in [0, 1], \tag{24}$$

with $t = 0.12$ the thickness. In this section, t is treated as a shape parameter. A linear Taylor series extrapolation in t-space is performed to predict the flow around a NACA 0015 airfoil using the flow and sensitivity data obtained from the baseline flow around a NACA 0012 airfoil.

Calculations are performed using 5th to 7th order Taylor series expansions on 6- to 8-layer patches to evaluate boundary derivatives in the sensitivity boundary conditions. As can be seen from figure 4, the degree of the Taylor series and the extent of the patch have little effect on the sensitivity fields for the finest grids. Eight grid adaptation cycles are performed, with the last mesh containing roughly 40 000 nodes (figure 5). All flow and sensitivity variables contribute to the error estimation and mesh adaptation processes. From here we only present results obtained with 7th order Taylor series expansions evaluated on 8-layer patches.

Figure 6 shows the baseline pressure coefficient along the surface of the NACA 0012 airfoil, its Taylor series extrapolation to that of a NACA 0015 airfoil and the pressure coefficient from a flow analysis for a NACA 0015 airfoil. As can be seen, the agreement is very good. The pressure coefficient on the pressure side of the airfoil is predicted very accurately. For the suction side, trends are well predicted. However, there is a slight discrepancy in the suction peak between the Taylor series and the reanalysis. This indicates that the pressure coefficient is a nearly linear function of t on the pressure side and exhibits a slighlty higher degree behavior on the suction side of the airfoil.

Figure 7 shows comparisons for the pressure fields in the vicinity of the airfoil, for the NACA 0012 baseline, its Taylor series extrapolation to a NACA 0015 and the contours from a reanalysis of the flow around a NACA 0015 airfoil. Again, a very satisfactory agreement is obtained between the extrapolated pressure field and the pressure field obtained from a new computation.

The velocity field is characterized by a large recirculation zone near the trailing edge of the airfoil. The

size and shape of this recirculation bubble are influenced by the thickness of the airfoil. Therefore, the geometrical characteristics of the bublle are a demanding criterion to assess the capability of the proposed approach to predict nearby solutions. The figure 8 shows the streamlines for the different computations. For the baseline NACA 0012 airfoil (figure 8(a)), a large recirculation zone is observed on the suction side close to the trailing edge. A second smaller recirculation is also present just downstream of the trailing edge. The Taylor series estimate for a NACA 0015 airfoil properly predicts the size increase for the two recirculation bubbles (figure 8(b)). The upper bubble is shifted upwards as the lower bubble increases in length. Results from a flow reanalysis around a NACA 0015 airfoil are shown in figure 8(c). As can be seen from figures 8(b) and 8(c), the characteristics of the recirculation zones are well predicted by the Taylor series extrapolation. In particular, the changes in the length and shape of the recirculation zone are especially well predicted by the sensitivities.

5.3 Angle of attack

We now consider the angle of attack as a shape parameter. We use linear Taylor series to predict the flow at $\alpha = 6^\circ$ from the baseline solution and sensitivity information obtained at $\alpha = 5^\circ$. The angle of attack is modified by rotating the whole airfoil around its leading edge. All calculations use 7th order Taylor series expansions and 8-layer patches for boundary derivatives extraction.

The figure 9 presents a comparison of the pressure coefficient on the airfoil for the baseline flow, its extrapolation from $\alpha = 5^\circ$ to $\alpha = 6^\circ$ and a new computation at $\alpha = 6^\circ$. Results show that wall pressure changes due to a 1° perturbation in α are well predicted by the linear extrapolation, for both sides of the airfoil. If we compare the whole pressure fields in the vicinity of the airfoil (figure 10), we observe that the trend is satisfactorily predicted by the sensitivity analysis.

Finally, the comparison of the streamlines (figure 11) proves the capability of the present approach to predict the flow changes in the near wake due to changes in α.

5.4 Camber

As a third exercise, we consider the modification of the camber of the airfoil. For a NACA XY12 airfoil, the mean line of the airfoil is described by two parabolic curves, whose maxima are joined and located at Y tenths of the chord and have the value of X percent of the chord. For example, the equation of the mean line for a NACA 4512 airfoil is provided by a single equation:

$$y = -\gamma(x^2 - x) \quad x \in [0, 1], \tag{25}$$

with $\gamma = 0.16$ the amplitude coefficient. The thickness distribution given by equation (24) is added to the mean camber to obtain points on the surface of the NACA 4512 airfoil.

New calculations are performed, using γ as a shape parameter, to predict the flow around a NACA 4512 airfoil using the baseline flow and sensitivities computed around a NACA 0012 airfoil. Computations are performed using 7th order Taylor series and 8-layer patches for the extraction of flow derivatives at the boundary.

The results presented on figures 12 to 14 indicates that this problem exhibits a more complex behavior that is not linear in γ. The overall characteristics of the flow are well predicted, but the discrepancies between the extrapolation and the computation at perturbed values of the parameter increase, underlining the non-linear nature of the flow field response to changes in the camber. In particular, the recirculation length is clearly under-estimated by the linear Taylor series (figure 14) while too high a suction peak is predicted (figure 12).

6 Application to uncertainty analysis

Finally, the CSEM is used to evaluate uncertainties of the flow fields due to uncertainties in geometrical parameters. We now consider several geometrical parameters simultaneously $(a_i)_{i=1,n}$ whose values are uncertain. Thus $a_i = a_i^0 + \Delta a_i$, where a_i^0 is the nominal value of a_i and Δa_i its uncertainty. The

uncertainties of the flow fields can be quantified by the first order statistics[4]:

$$\begin{aligned}(\Delta u)^2 &\approx \sum_i (\frac{\partial u}{\partial a_i}\Delta a_i)^2 \\ (\Delta v)^2 &\approx \sum_i (\frac{\partial v}{\partial a_i}\Delta a_i)^2 \\ (\Delta p)^2 &\approx \sum_i (\frac{\partial p}{\partial a_i}\Delta a_i)^2 \end{aligned} \tag{26}$$

Cascading input data uncertainty through the CFD code to obtain uncertainty estimates of the flow response puts CFD on par with experimental procedures which have been reporting such uncertainties for decades. CFD uncertainty intervals make comparison with experimental data a more rigorous exercise.

Uncertainty analysis is applied to a NACA 0012 airfoil, subject to uncertainties in the thickness $|\Delta t|$, the angle of attack $|\Delta\alpha|$ and the camber $|\Delta\gamma|$. The uncertainties of these parameters are supposed to be small with respect to the parameter value. For demonstration purposes, we assume the following values for an airfoil of chord length l:

$$|\Delta t| = 0.01l \quad |\Delta\alpha| = 0.5^\circ \quad |\Delta c| = 0.01l \tag{27}$$

Uncertainty analysis is performed using equations (26) and sensitivity fields computed as in the previous sections for the baseline flow.

Figure 15 shows uncertainties distributions over the whole flow fields. As can be seen, the uncertainties on the pressure p are mainly located at the suction peak, where the pressure intensity is the highest. Notice that the pressure uncertainties in the recirculation zone are small. The largest uncertainties for u are located in the vicinity of the airfoil, since any change in the wall position will strongly modify the velocity profiles. As one would expect, large uncertainties in the airfoil wake are also predicted. This is not the case for the uncertainties on the v-component of velocity. The largest uncertainties are located close to the leading edge of the airfoil, where high values of v are encountered.

The analysis now focuses on the uncertainties on the pressure coefficient C_p along the airfoil and the uncertainties on u in the wake. The uncertainties of the pressure coefficient are shown in figure 16. Solid lines represent the pressure coefficient computed for a NACA 0012 airfoil (nominal values of t, α and γ) and dashed lines represent the uncertainty interval induced by the parameter uncertainties around the

nominal prediction. As can be seen, the largest uncertainties are located near the suction peak and along the whole pressure side of the airfoil. However, uncertainties on the suction side are very small as one moves away from the suction peak. This behaviour is certainly related to the presence of the recirculation zone at this location. Sensitivity information provide the means of identifying the individual contribution of each parameter to the overall uncertainty. This provides a rigorous tool to identify which parameter has the most influence on the overall uncertainty (figure 17). On the suction side, the uncertainties on C_p near the suction peak caused by the thickness uncertainty are far larger than the uncertainty induced by camber or angle of attack. On the remainder of the suction side, the uncertainties due to the three parameters are of similar magnitude. On the pressure side, airfoil thickness plays the main role in the mid-part of the airfoil, whereas the uncertainties caused by that of the angle of attack are larger in the vicinity of the leading edge and trailing edge. The uncertainties due to camber play a lesser role in this case.

Consider now the uncertainty on u in the wake of the airfoil. Figure 18 shows the uncertainty band for u at a x-station located one chord downstream of the airfoil. As observed, the uncertainty band is wider in the central part of the wake and becomes progressively narrower in the freestream. The wake uncertainty is decomposed in individual parameter contributions in figure 19. For the three parameters, the uncertainties for u vanish at precise locations close to the center of the wake, but at different points. It is interesting to observe that, this time, the uncertainty due to camber is the most important. This trend is opposite to that observed for the pressure coefficient. The uncertainty on u due to that of the thickness is particularly small. For the upper part of the wake, the uncertainties due to camber uncertainty are dominant, whereas for the lower part of the wake, the uncertainties due to the angle of attack uncertainty are larger. Thus, this approach allows us to quantify the uncertainties of the flow fields and to identify the individual contribution of each geometrical parameter.

CONCLUSION

A Continuous Sensitivity Equation Method (CSEM) has been developed for shape parameters. We introduced a Taylor series l-patches constrained least-squares procedure to evaluate the flow gradients which appear in the CSE boundary conditions. Flow and sensitivity fields were solved using an adaptive finite-element method.

The proposed approach was applied to fast evaluation of nearby flow solutions around NACA-series airfoils of varying shape. Comparisons between fast evaluations by Taylor series in parameter space and reanalysis have shown good agreements when the thickness, the angle of attack and the camber are considered as shape parameters. The ability of the proposed method to predict the changes in the pressure field or the wake characteristics due to shape changes was demonstrated. Finally, the CSEM is used to assess the level of uncertainty in the flow fields due to geometrical uncertainties of a NACA 0012 airfoil. Particularly, the uncertainties of the pressure coefficient and the first component of the velocity in the wake, due to the uncertainties of thickness, angle of attack and camber have been quantified.

A Boundary conditions for the CSE

We detail the boundary conditions for the CSE when the thickness, the angle of attack and the camber are considered as sensitivity parameters. The boundary conditions for the sensitivity fields are obtained by differentiating the boundary conditions for the flow with respect to the sensitivity parameters. Since only the airfoil boundary is parameter dependent, the boundary conditions imposed on the outer boundary can be easily derived. At the inlet, where a Dirichlet boundary condition is imposed for the flow, we obtain:

$$\begin{aligned} s_u &= 0 \\ s_v &= 0. \end{aligned} \tag{28}$$

At the outlet, where an homogeneous Neumann boundary condition is imposed for the flow ($t_x = 0$ and $t_y = 0$), the same kind of boundary condition is derived for the sensitivity fields:

$$\begin{aligned} t'_x &= 0 \\ t'_y &= 0, \end{aligned} \tag{29}$$

Where t'_x and t'_y are the surface force sensitivities. At the airfoil boundary, the boundary conditions for the CSE depend on the parameter considered.

A.1 Thickness

For the flow, a Dirichlet boundary condition is imposed on the airfoil, since the fluid velocity vanishes at the wall. According to equation (9), the corresponding boundary condition at the boundary point $P(x_P, y_P)$ for the sensitivities with respect to the thickness t is:

$$\begin{aligned} s_u &= -(u_x \frac{\partial x_P}{\partial t} + u_y \frac{\partial y_P}{\partial t}) \\ s_v &= -(v_x \frac{\partial x_P}{\partial t} + v_y \frac{\partial y_P}{\partial t}). \end{aligned} \tag{30}$$

The partial derivatives of the wall position with respect to the thickness is obtained by differentiating equation (24), which yields:

$$\begin{aligned} s_u &= -u_y \times 5(0.2969\sqrt{x}_P - 0.1260x_P - 0.3537x_P^2 + 0.2843x_P^3 - 0.1015x_P^4) \\ s_v &= -v_y \times 5(0.2969\sqrt{x}_P - 0.1260x_P - 0.3537x_P^2 + 0.2843x_P^3 - 0.1015x_P^4). \end{aligned} \tag{31}$$

A.2 Angle of attack

The modification of the angle of attack α is performed by rotating the airfoil around its leading edge. Thus, similar manipulations yield the following boundary condition for the sensitivities on the airfoil:

$$\begin{aligned} s_u &= -u_x \times y_P + u_y \times x_P \\ s_v &= -v_x \times y_P + v_y \times x_P. \end{aligned} \tag{32}$$

A.3 Camber

When the coefficient γ is considered as the parameter to modify the camber, the partial derivatives of the wall position with respect to γ are obtained by differentiating equation (25):

$$\begin{aligned} s_u &= -u_y \times (x_P^2 - x_P) \\ s_v &= -v_y \times (x_P^2 - x_P). \end{aligned} \tag{33}$$

References

[1] R. Duvigneau and D. Pelletier. Evaluation of nearby flows by a shape sensitivity equation method. In *43rd AIAA Aerospace Sciences Meeting and Exhibit*, Reno, NV, January 2005. AIAA Paper 2005–0127.

[2] É. Turgeon, D. Pelletier, and J. Borggaard. A continuous sensitivity equation approach to optimal design in mixed convection. *Numerical Heat Transfer*, 38:869–885, 2000.

[3] É. Turgeon, D. Pelletier, and J. Borggaard. Sensitivity and uncertainty analysis for variable property flows. In *39th AIAA Aerospace Sciences Meeting and Exhibit*, Reno, NV, Jan. 2001. AIAA Paper 2001-0139.

[4] M.M. Putko, P.A. Newman, A.C. Taylor, and L.L. Green. Approach for uncertainty propagation and robust design in cfd using sensitivity derivatives. In *15th AIAA Computational Fluid Dynamics Conference*, Anaheim, CA, June 2001. AIAA Paper 2001-2528.

[5] A. Jameson, L. Martinelli, and N. A. Pierce. Optimum aerodynamic design using the Navier-Stokes equation. *Theorical and Computational Fluid Dynamics*, 10:213–237, 1998.

[6] W. K. Anderson and V. Venkatakrishnan. Aerodynamic design optimization on unstructured grids with a continuous adjoint formulation. *Computers and Fluids*, 28(4):443–480, 1999.

[7] J. Elliott and J. Peraire. Practical 3d aerodynamic design and optimization using unstructured grids. *AIAA Journal*, 35(9):1479–1485, 1997.

[8] M.B. Giles, M.C. Duta, J.-D. Muller, and N.A. Pierce. Algorithm developments for discrete adjoint methods. *AIAA Journal*, 41(2), 2003.

[9] Joaquim R. R. A. Martins, Ilan M. Kroo, and Juan J. Alonso. An automated method for sensitivity analysis using complex variables. *AIAA Paper* 2000-0689, January 2000.

[10] B. Mohammadi and O. Pironneau. Mesh adaptation and automatic differentiation in a cad-free framework for optimal shape. *International Journal for Numerical Methods in Engineering*, 30(2):127–136, May 1999.

[11] F. Beux and A. Dervieux. A hierarchical approach for shape optimization. Technical Report 1868, Rapport de Recherche INRIA, 1993.

[12] J. Borggaard and A. Verma. On efficient solutions to the continuous sensitivity equation using automatic differentiation. *SIAM Journal on Scientific Computing*, 22(1):39–62, 2001.

[13] O. C. Zienkiewicz and J. Z. Zhu. The superconvergent patch recovery and *a posteriori* error estimates. Part 1: The recovery technique. *International Journal for Numerical Methods in Engineering*, 33:1331–1364, 1992.

[14] D. Pelletier, É. Turgeon, S. Etienne, and J. Borggaard. Reliable sensitivity analysis via an adaptative sensitivity equation method. In *3rd AIAA Theorical Fluid Mechanics Meeting*, St Louis, MO, Jun. 2002. AIAA Paper 2002-2758.

[15] D. Pelletier. Adaptive finite element computations of complex flows. *International Journal for Numerical Methods in Fluids*, 31:189–202, 1999.

[16] D. Pelletier and F. Ilinca. Adaptive remeshing for the $k - \epsilon$ model of turbulence. *AIAA Journal*, 35(4):640–646, 1997.

[17] O. C. Zienkiewicz and J. Z. Zhu. The superconvergent patch recovery and *a posteriori* error estimates. Part 2: Error estimates and adaptivity. *International Journal for Numerical Methods in Engineering*, 33:1365–1382, 1992.

[18] J. Peraire, M. Vahdati, K. Morgan, and O.C. Zienkiewicz. Adaptive remeshing for compressible flow computations. *Journal of Computational Physics*, 72(2):449–466, 1987.

[19] Y. Belhamadia, A. Fortin, and E Chamberland. Anisotropic mesh adaptation for the solution of the stefan problem. *J. Comp. Physics*, 194(1):233–255, 2004.

[20] D. Pelletier and P.J. Roache. CFD code verification and the Method of Manufactured Solutions. In *Proceedings of the 10th Annual Conferenceof the CFD Society of Canada*, Windsor, ON, June 9–11 2001.

List of Figures

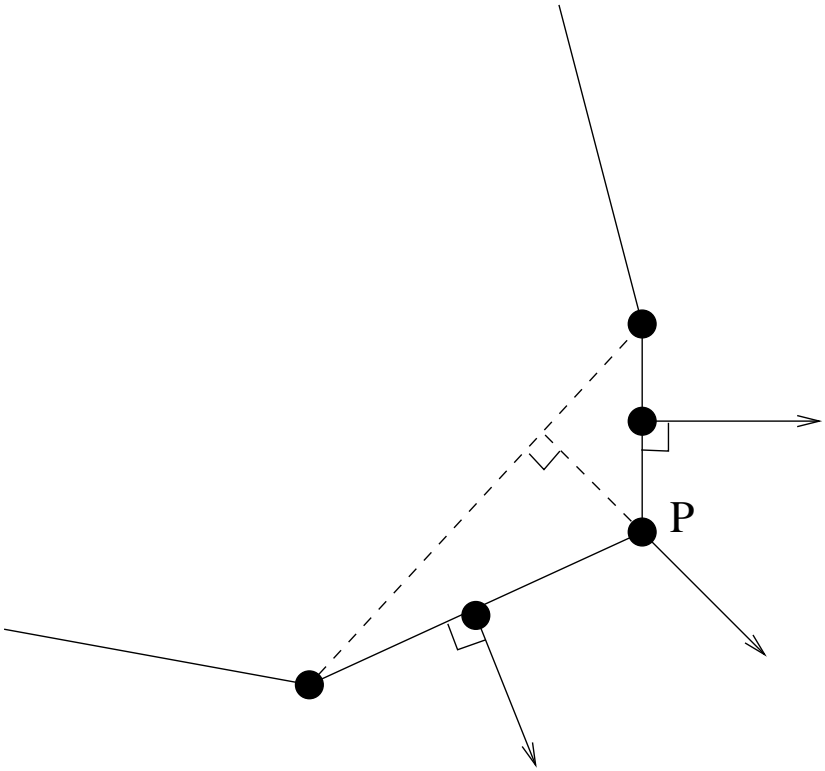

Figure 1: Definition of the normal vector at a vertex node.

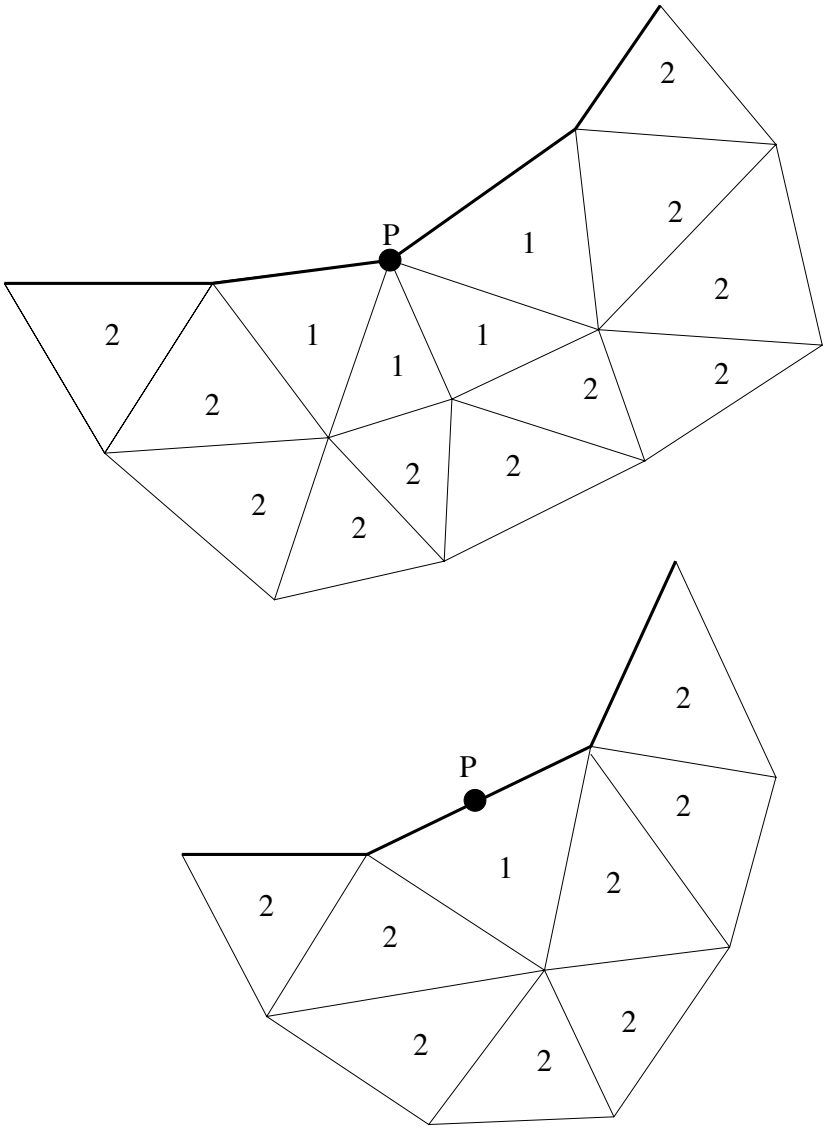

Figure 2: Typical 2-layer patches around node **P**.

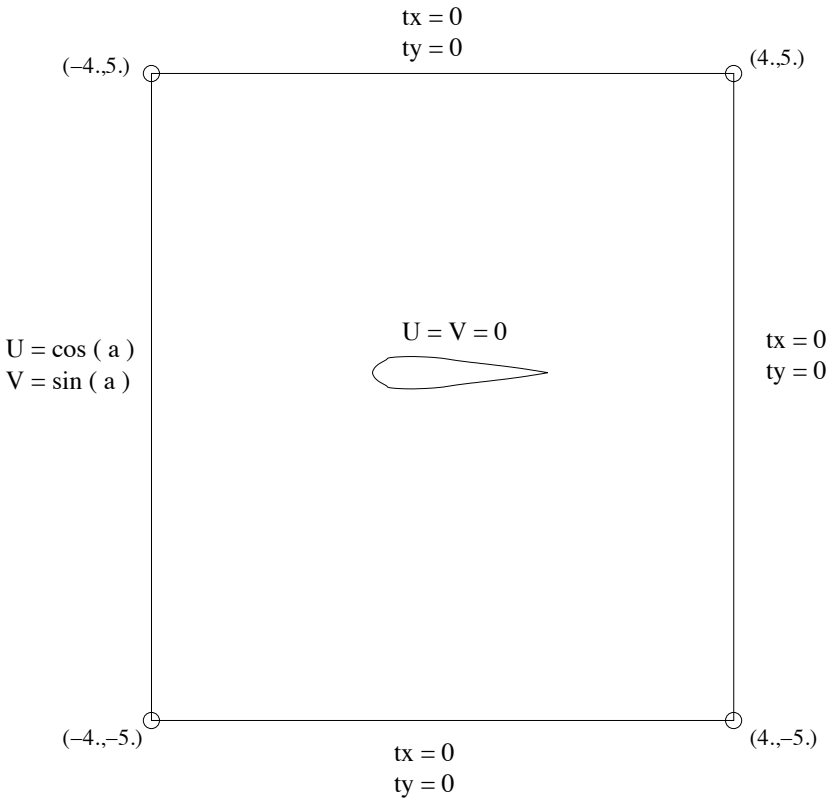

Figure 3: Computational domain around a NACA 0012 airfoil.

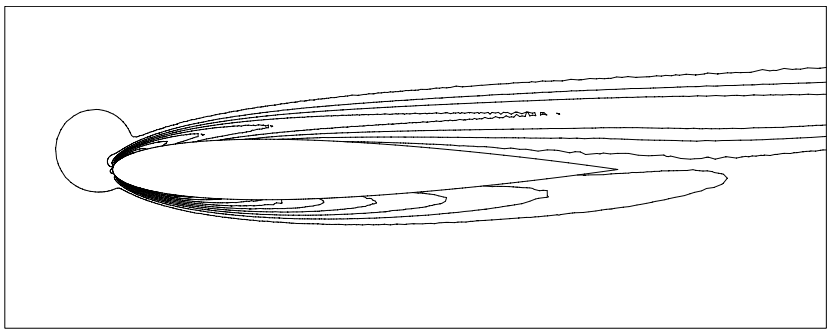

(a) 5th order on 6-layer patches

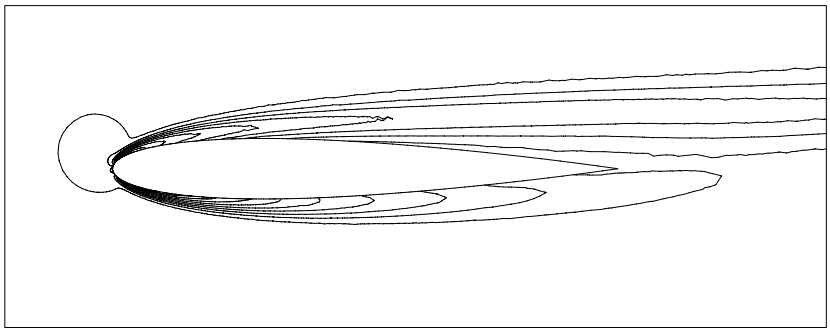

(b) 6th order on 7-layer patches

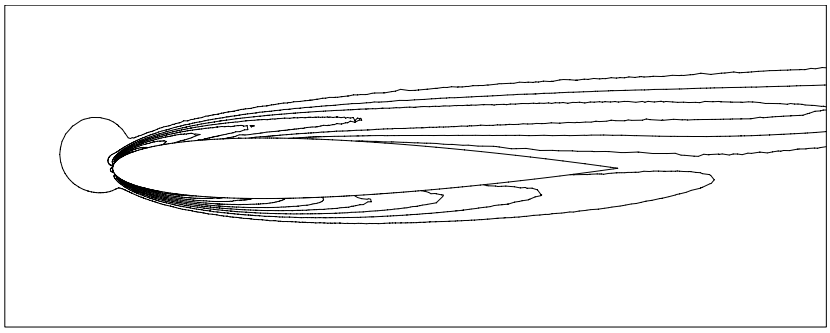

(c) 7th order on 8-layer patches

Figure 4: Effects of Taylor series order on S_u.

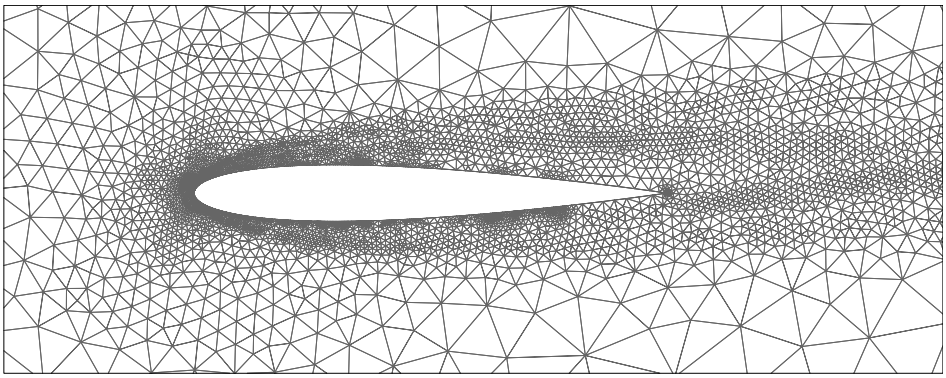

Figure 5: Typical adapted grid around a NACA 0012 airfoil.

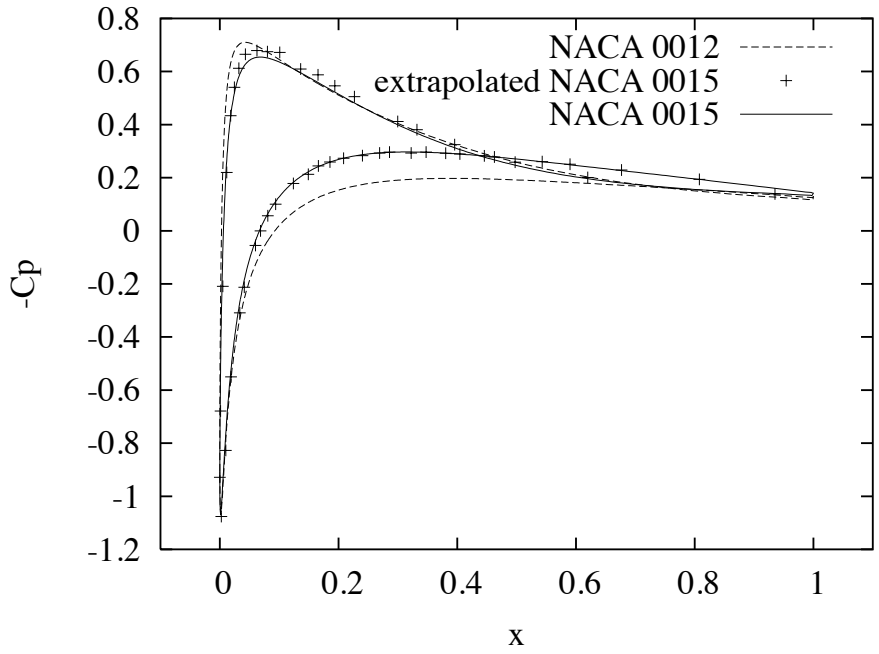

Figure 6: Comparison of the pressure coefficient for thickness modification.

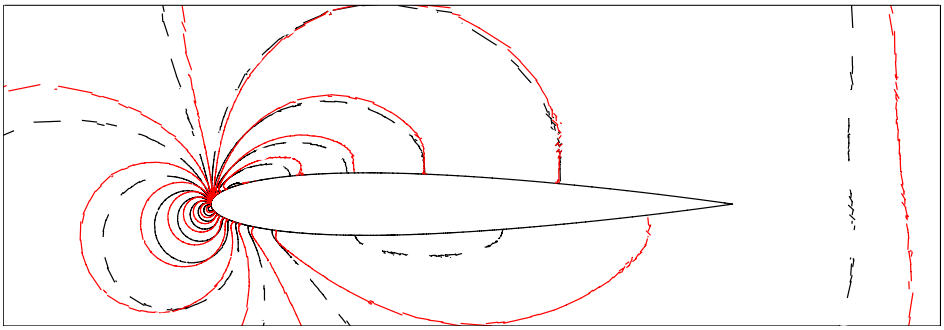

(a) NACA 0012 (dashed) and extrapolated to NACA 0015 (solid)

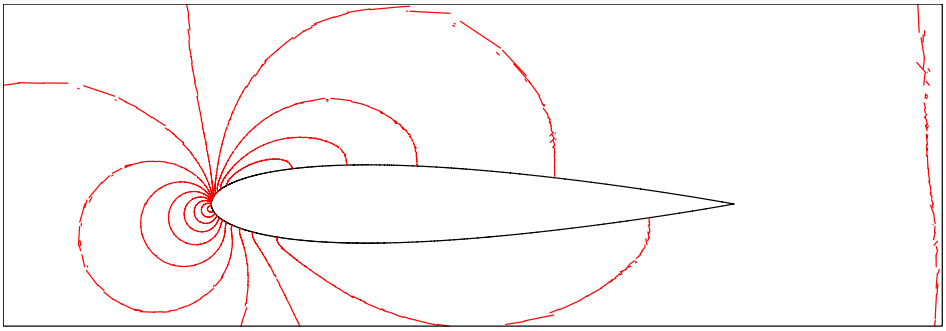

(b) NACA 0015

Figure 7: Comparison of pressure contours for thickness modification.

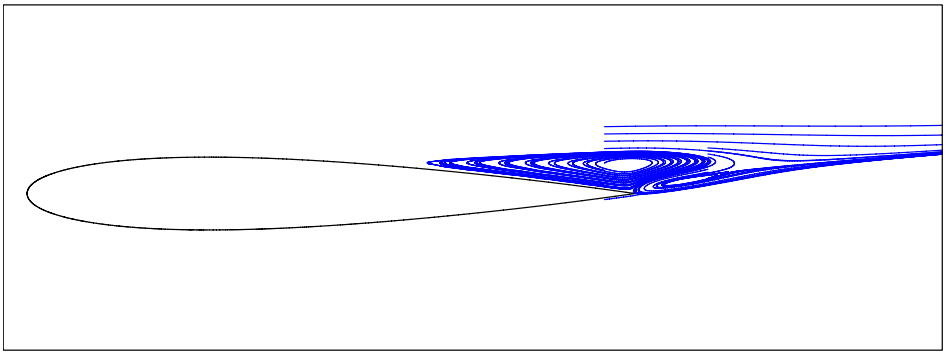

(a) NACA 0012

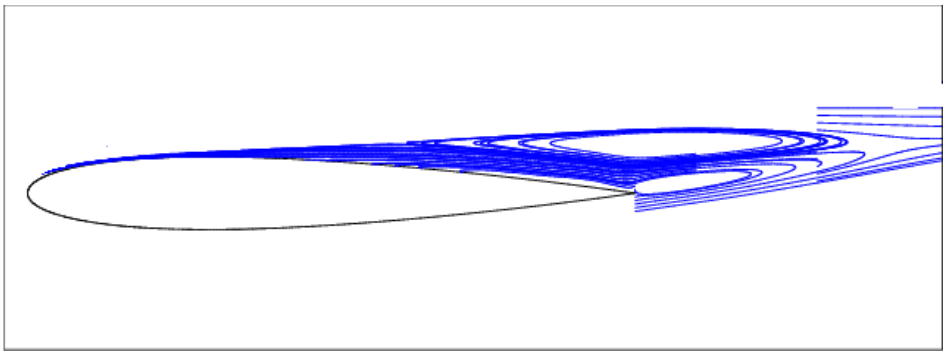

(b) Extrapolated to NACA 0015

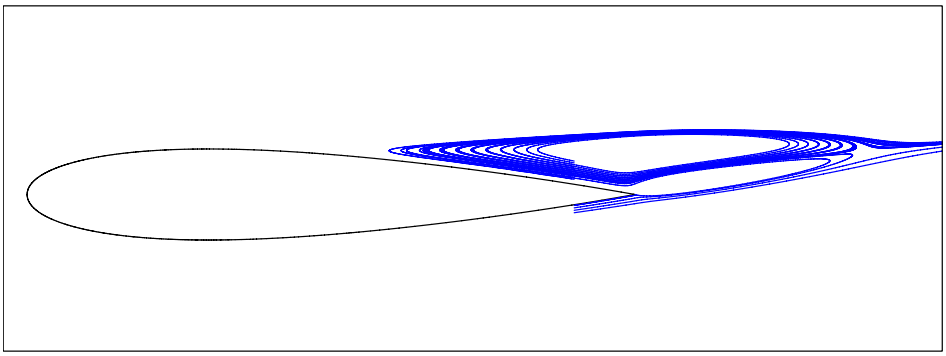

(c) NACA 0015

Figure 8: Comparison of streamlines in the recirculation zone for thickness modification.

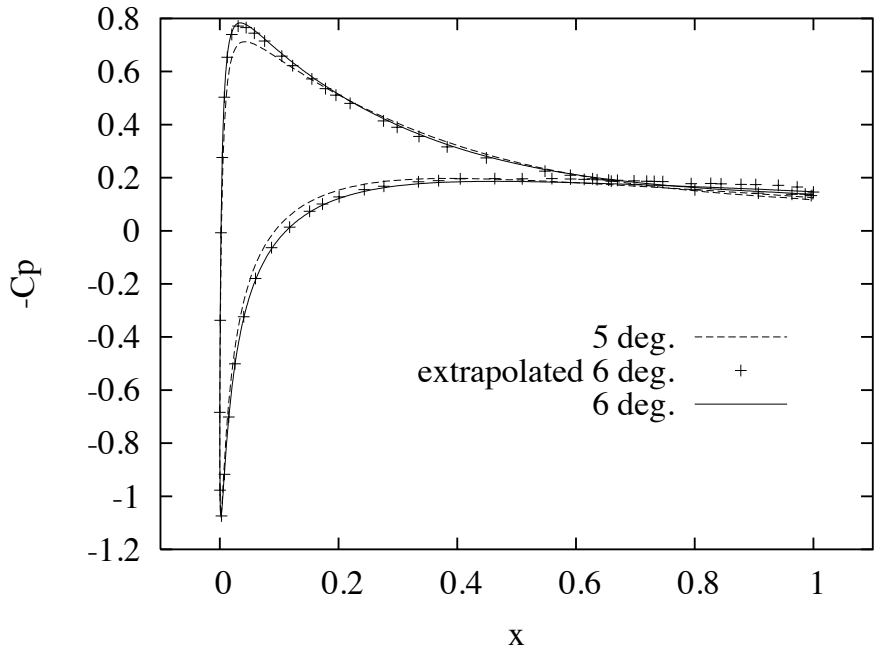

Figure 9: Comparison of the pressure coefficient for incidence modification.

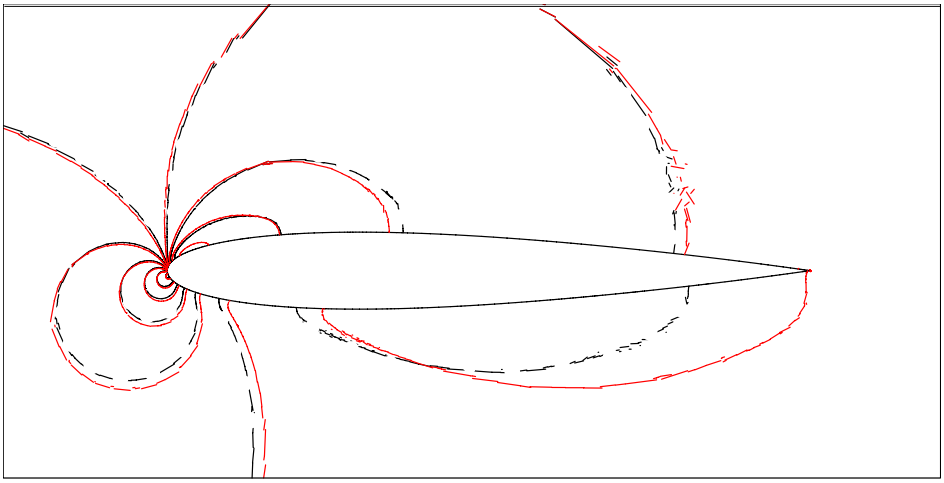

(a) $\alpha = 5°$ (dashed) and extrapolated to $\alpha = 6°$ (solid)

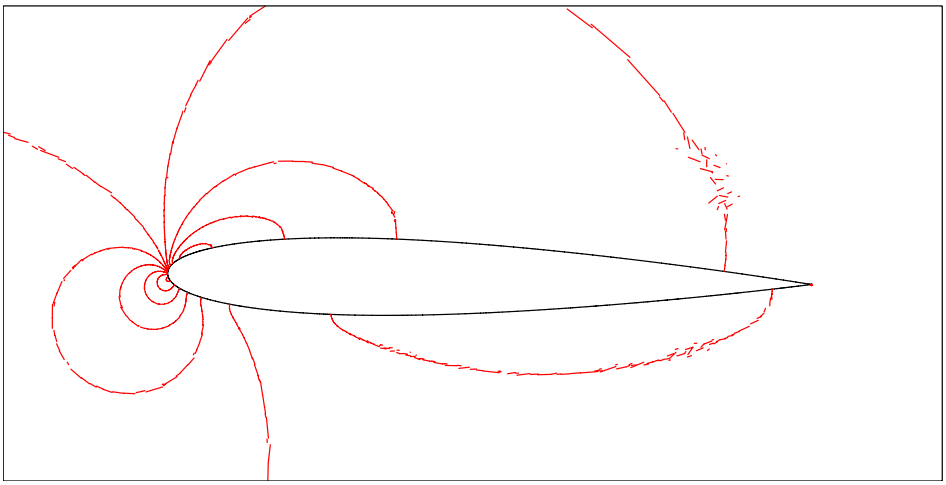

(b) $\alpha = 6°$

Figure 10: Comparison of pressure contours for incidence modification.

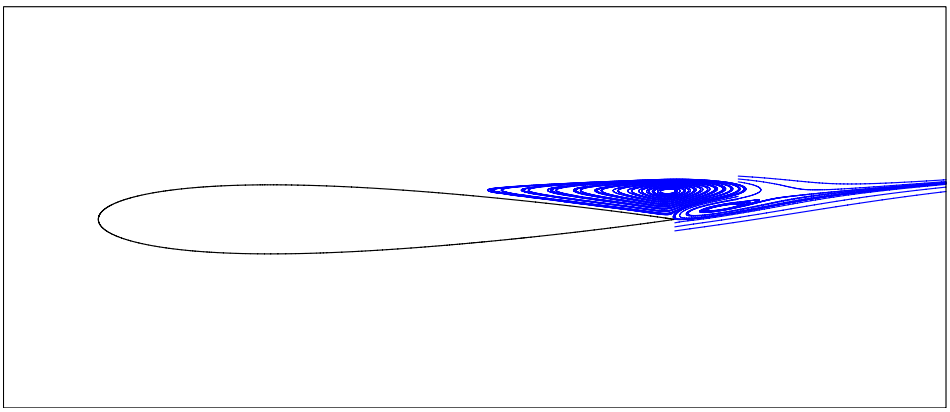

(a) $\alpha = 5°$

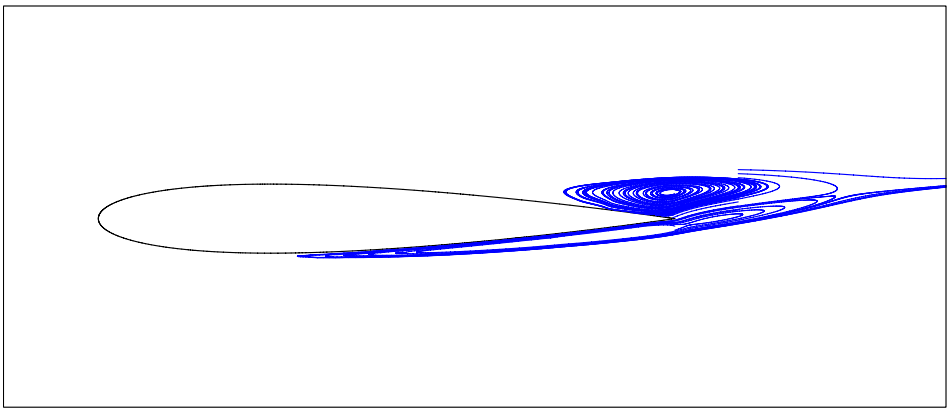

(b) Extrapolated to $\alpha = 6°$

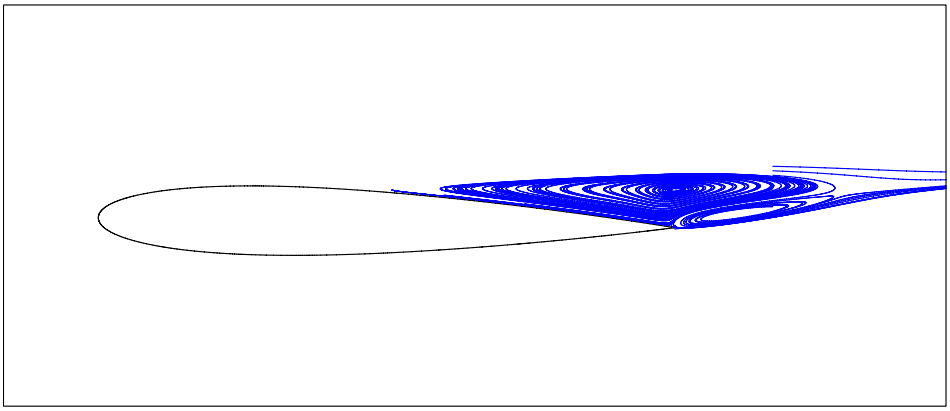

(c) $\alpha = 6°$

Figure 11: Comparison of the streamlines in the recirculation zone for incidence modification.

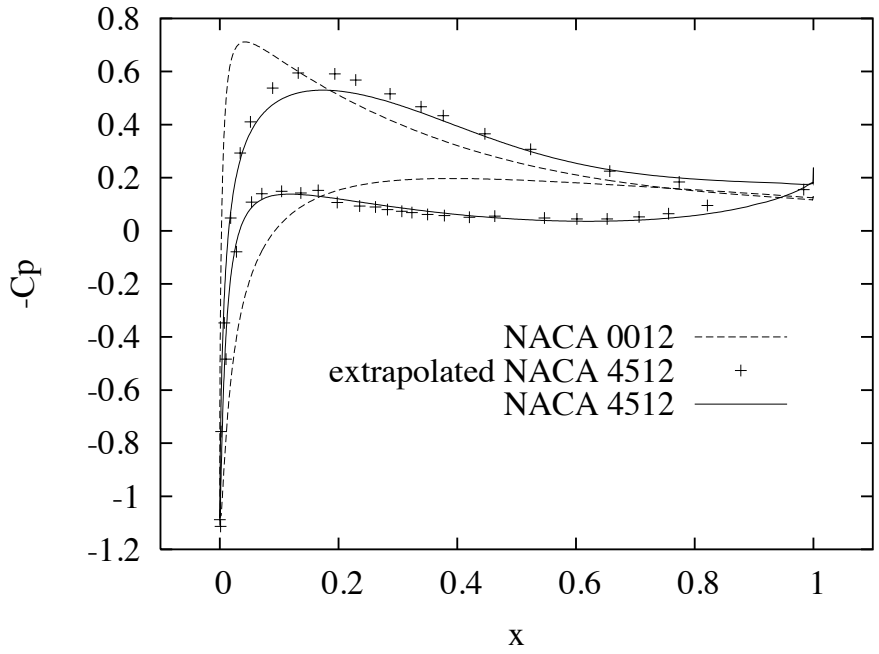

Figure 12: Comparison of the pressure coefficient for camber modification.

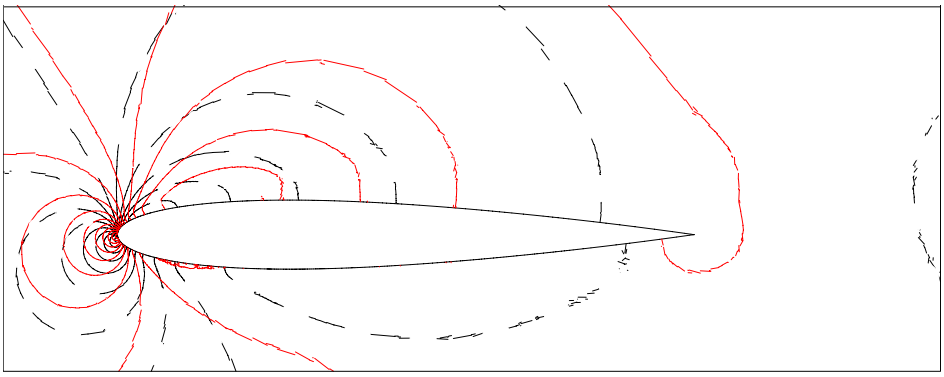

(a) NACA 0012 (dashed) and extrapolated to NACA 4512 (solid)

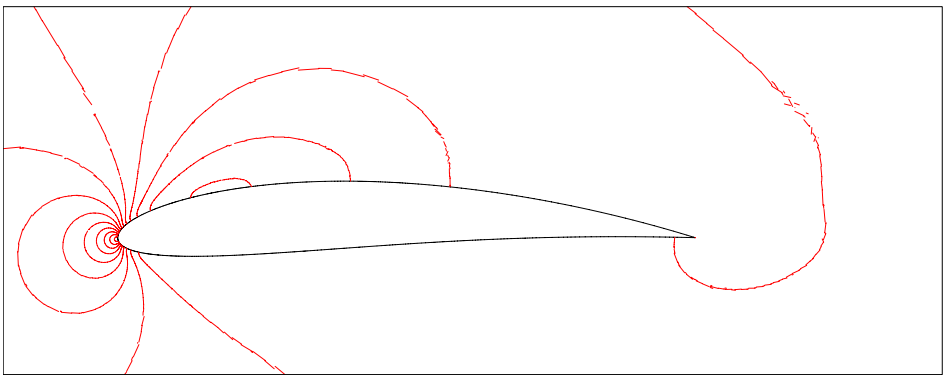

(b) NACA 4512

Figure 13: Comparison of pressure contours for camber modification.

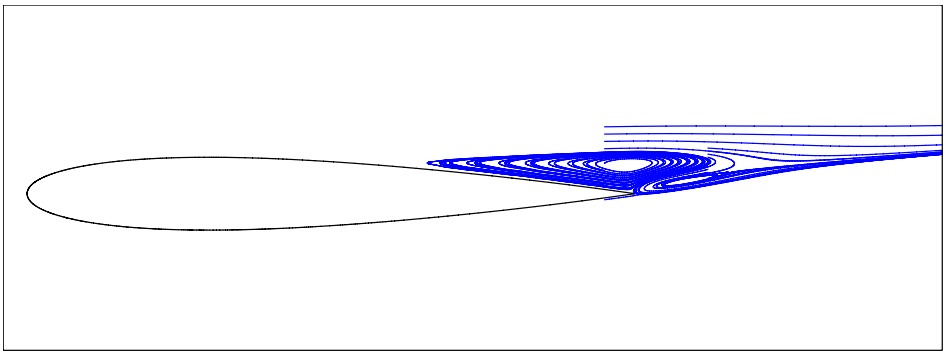

(a) NACA 0012

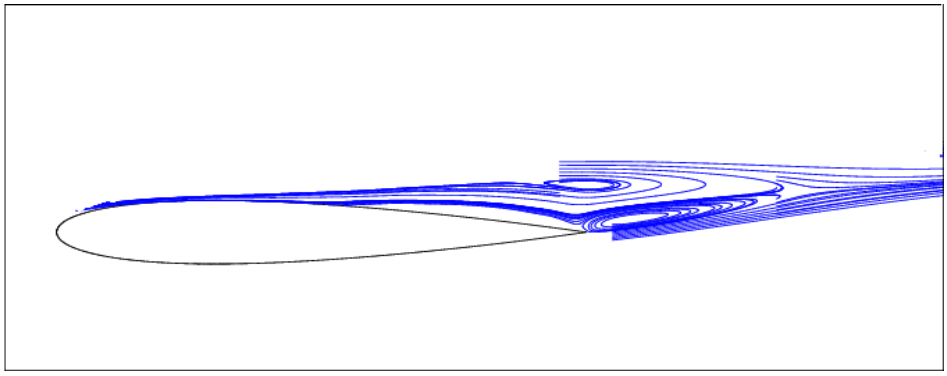

(b) Extrapolated to NACA 4512

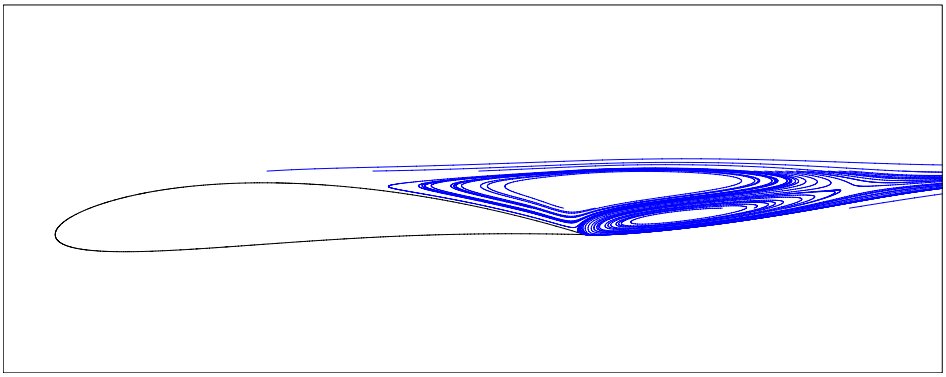

(c) NACA 4512

Figure 14: Comparison of the streamlines in the recirculation zone for camber modification.

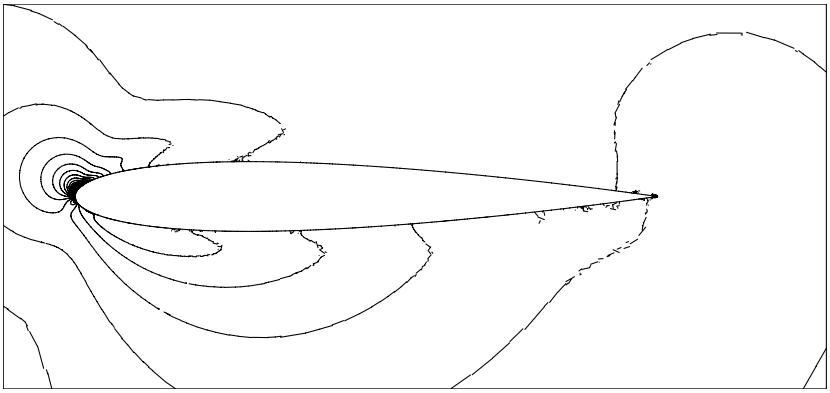

(a) $|\Delta p|$

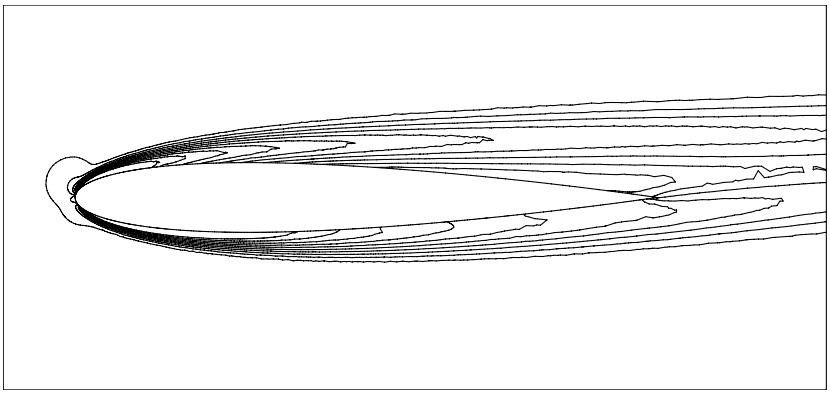

(b) $|\Delta u|$

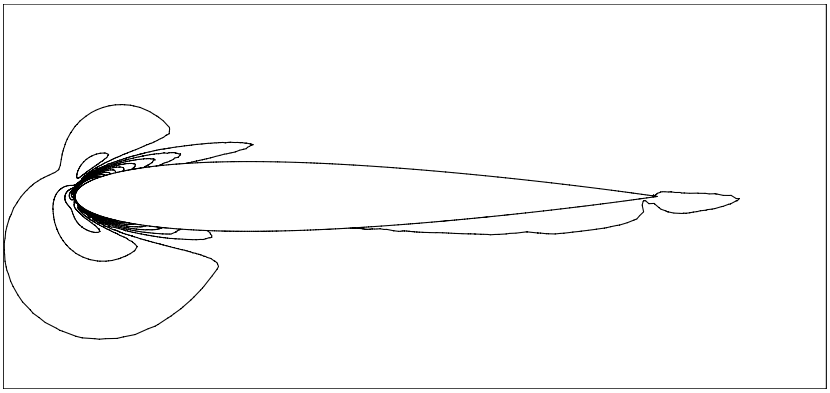

(c) $|\Delta v|$

Figure 15: Uncertainties in the flow field.

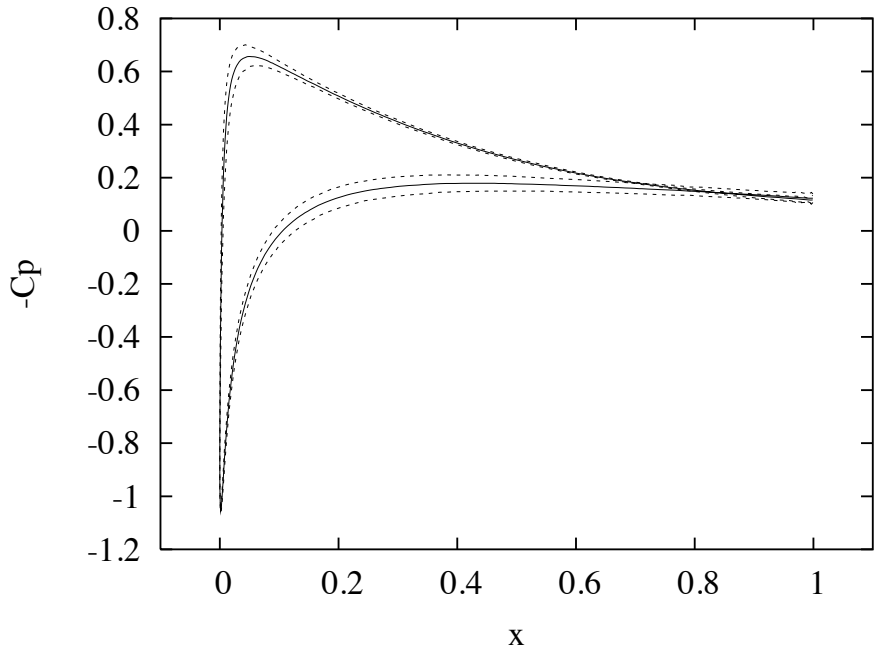

Figure 16: Uncertainty band for the pressure coefficient.

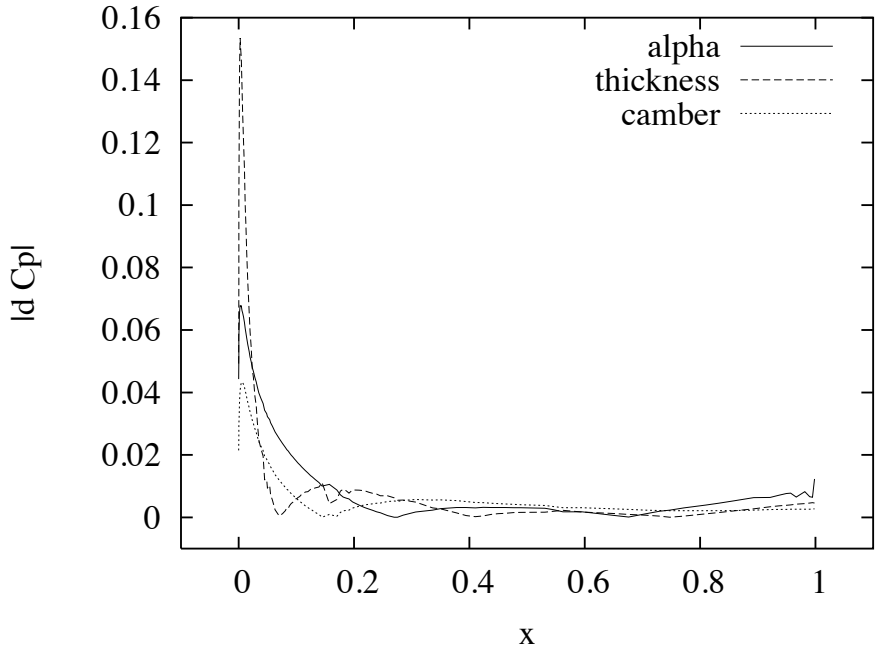

(a) Suction side

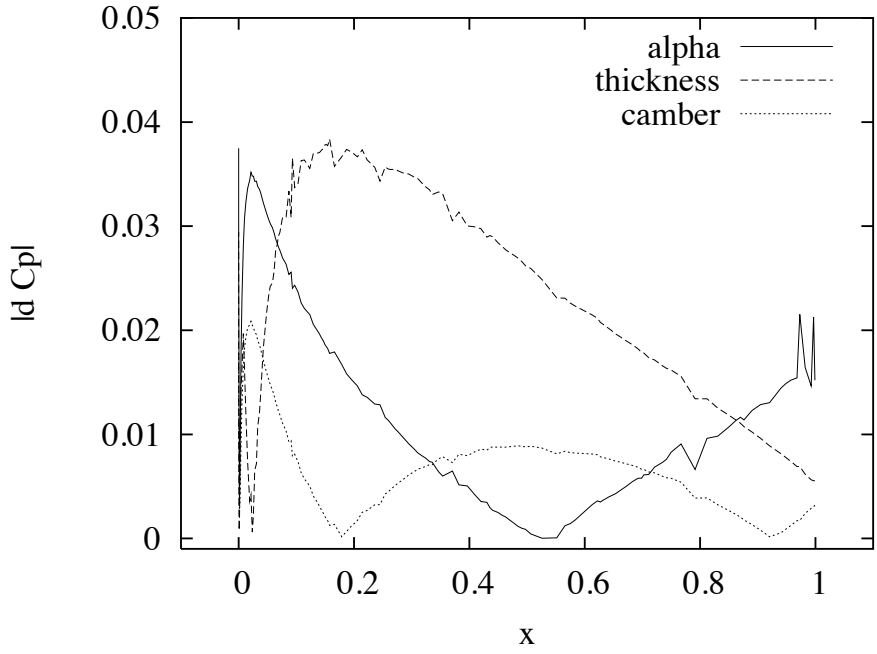

(b) Pressure side

Figure 17: Individual contributions to total uncertainty.

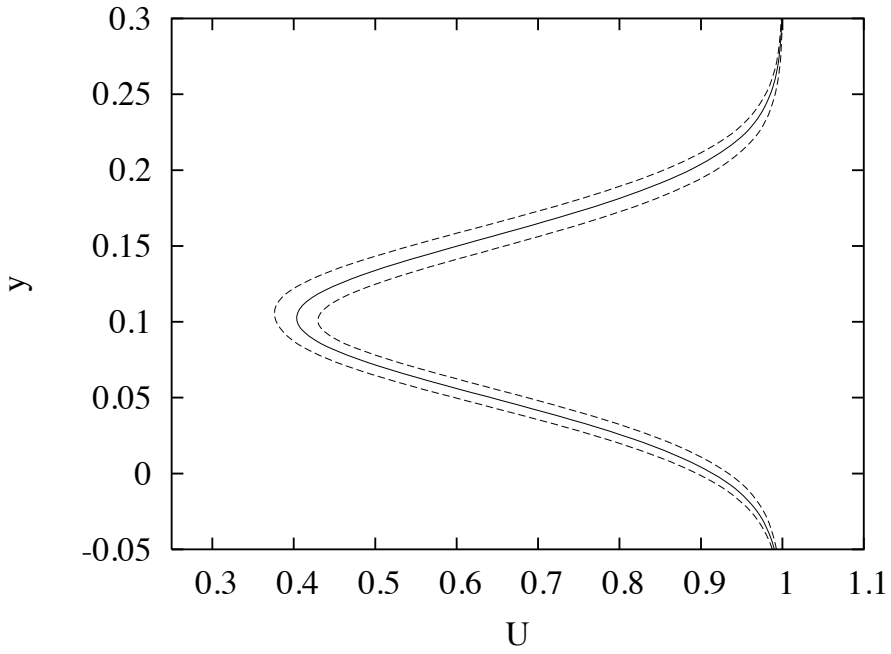

Figure 18: Uncertainty band for u in the wake.

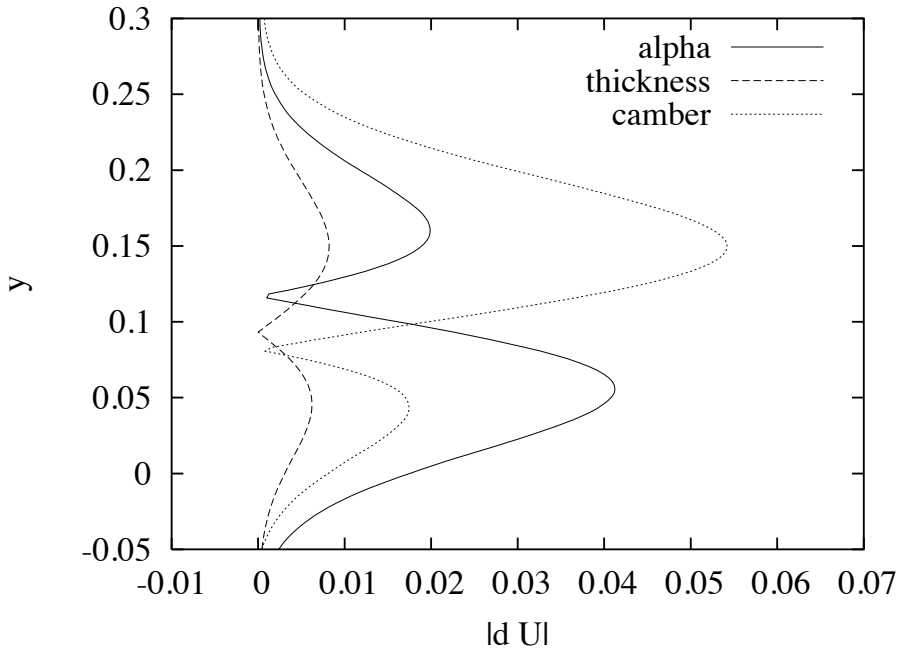

Figure 19: Individual contributions to total uncertainty.